Modeling porosity migration in LWR and fast reactor MOX fuel using the finite element method

Stephen Novascone [a, *], Pavel Medvedev [a], John W. Peterson [b], Yongfeng Zhang [a], Jason Hales [a]

[a] Fuels Modeling and Simulation, Idaho National Laboratory, Idaho Falls, ID, 83415, USA
[b] Modeling and Simulation, Idaho National Laboratory, Idaho Falls, ID, 83415, USA

ARTICLE INFO

ABSTRACT

An engineering-scale finite element simulation of pore migration in oxide fuel is presented. The porosity field is governed by an advection-diffusion equation which is coupled to the fuel temperature and stress fields through the thermal conductivity and volumetric heat source term. The engineering-scale porosity equation models the microscopic process of vapor transport of fuel across pores, taking into account thermal and vapor pressure gradients within the fuel. In the simulations, the porosity is initialized to a constant value at every point in the domain, and as the temperature gradient is increased by application of a heat source, the pores move up the thermal gradient and accumulate at the center of the fuel in a time frame that is consistent with experimental observations. Results from representative simulations are provided to demonstrate the new capability, and we show that a sufficiently high power ramp rate limits restructuring and leads to a corresponding increase in fuel temperature. We also discuss the finite element mesh density required to compute pore migration and present multidimensional results.

1. Introduction

After start-up and attainment of full-power and nominal operating temperature, ceramic, or oxide fuel (UO_2 and MOX) experiences micro- and engineering-scale restructuring, which has a profound effect on the bulk properties of the fuel [1]. Restructuring mostly affects MOX fuel in fast reactors due to the higher temperatures, but can be relevant to light water reactors if temperatures go outside of normal operating ranges [2], such as during a loss of coolant accident. As such, the objective of this study is to consider oxide fuel in general, using models from a variety of sources. Here, restructuring means that the fuel pellet develops distinct regions from fuel center to fuel surface. Going from the center of the fuel outward in sequence, these regions are characterized by a central void, a region of increased density, and then a region with radially aligned grains and un-restructured grains. These regions, which depend on both the temperature value and temperature gradient, form radial isosurfaces within the fuel. Fig. 1 shows a micrograph of MOX fuel with the central void, and Fig. 2 is a diagram highlighting the features of the micrograph. Both figures are from Olander [1].

The salient feature of restructuring is the movement of pores. Under large thermal gradients, pores introduced during fabrication are generally greater than 1 μm in size, and are uniformly distributed throughout the pellet. Pores move toward the center of the pellet where they eventually coalesce into a large central void. Speculation regarding the manner in which the central void forms has led to the concept of a vapor transport mechanism in which fuel at the surface of the hot side of a pore vaporizes, then condenses on the cool side of the pore. The result is a net flux of pores toward the pellet center. Theoretical support for the vapor transport mechanism comes from Nichols [3] and Sens [4]. The physical and mathematical models governing pore migration on the microscale are well-summarized in Ref. [5]. The emphasis in the present work is on the application of these models to engineering-scale finite element simulations.

2. Considerations of prior work

Examples of other fuel performance codes that have included the effects of pore migration include: CEPTAR [6], FEAST [7], GERMINAL [8,9], and LIFE4 [10]. These codes do not use the finite

* Corresponding author.
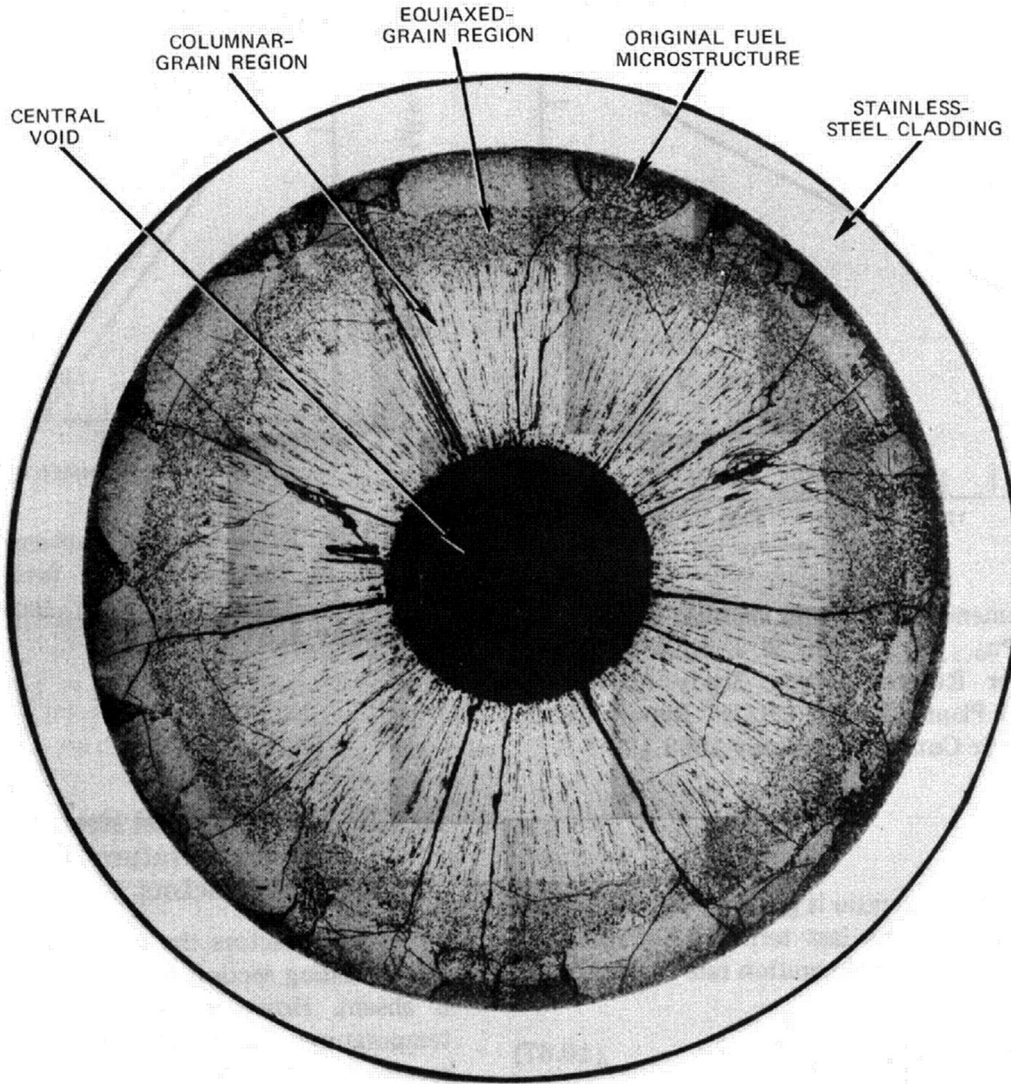   E-mail address: stephen.novascone@inl.gov (S. Novascone).

Fig. 1. Micrograph from Olander showing central void, restructured, and original fuel [1].

element method, are limited to 1D, and do not solve for all field variables simultaneously (i.e. they are not fully coupled). CEDAR [11] does use the finite element method to solve for displacements (stress divergence), but does not fully couple to temperature and porosity solutions. Since porosity and temperature are strongly coupled physical quantities, solving the governing equations in a fully coupled manner leads to increased confidence and fidelity in the results, and an improvement in the state of the art.

3. Mathematical model

In the following sections, we describe the model and our general approach, then show the results from specific calculations.

3.1. Field equations

To simulate pore migration, we are going to make use of three partial differential equations that model the variables temperature, porosity, and stress (displacements). The three equations come from applications of: i.) energy conservation (change in temperature), ii.) advection-diffusion of pores (conservation of pores), and ii.) stress divergence (static equilibrium). In mathematical form, the partial differential equations are:

$$\rho C \frac{\partial T}{\partial t} - \nabla \cdot k \nabla T - q = 0 \tag{1}$$

$$\frac{\partial p}{\partial t} + \nabla \cdot [(1-p)p\, \overrightarrow{v} - \nu \nabla p] = 0 \tag{2}$$

$$\nabla \cdot \boldsymbol{\sigma} = 0 \tag{3}$$

where ρ is density, C is specific heat capacity, k is thermal conductivity (a function of porosity and temperature), T is temperature, q is the heat source term, p is the porosity, $\overrightarrow{v}$ is the pore velocity, ν is an effective porosity diffusion coefficient to represent pore migration via surface and bulk diffusion, and $\boldsymbol{\sigma}$ is the stress tensor. The symbol ∇ is the del operator and changes form depending on the coordinate system. These equations are solved implicitly (fully coupled to each other), using the finite element formulation in the fuel performance code BISON [12], which is built on the MOOSE framework [13]. BISON uses standard SI units to represent all physical quantities; specific values for the properties in Equations (1)–(3) are given in subsequent sections.
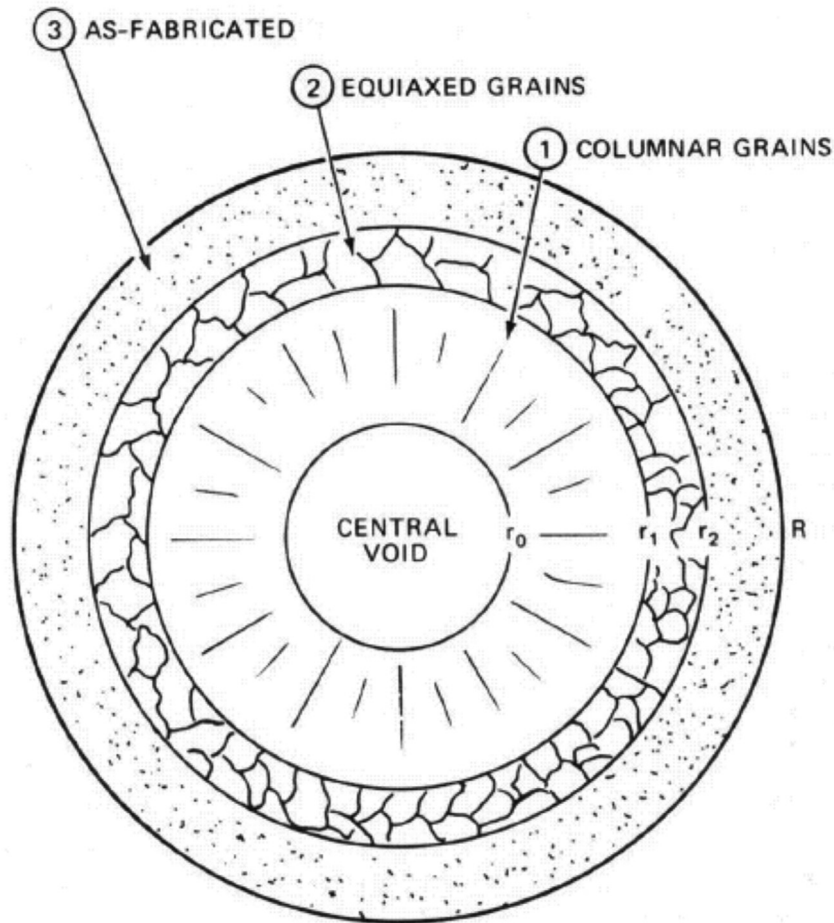
Fig. 2. Diagram of microscale features where equiaxed and columnar grain regions are distinguished [1].

In Equation (1), the thermal conductivity k and the volumetric heat source q are both porosity-dependent; more detail regarding these relationships is documented in subsequent sections.

In Equation (2), porosity is defined in terms of fraction of pores per unit volume. A value of $p = 1$ represents a void and $p = 0$ represents maximum mass density. The term $(1 - p)p$, multiplied by the pore velocity, is used to ensure that porosity is always between 0 and 1 and that the pore velocity term is active only for values of porosity that are between 0 and 1, which has physical meaning because pore movement is non-existent in regions full of pores ($p = 1$) and in regions without pores ($p = 0$).

Note that in Equation (2), the pore velocity $\vec{v}$ depends on the temperature, T. At the engineering scale, we view the concentration of individual pores within the fuel as a continuous field, and assume that this concentration changes (pore migration) due to both the pore velocity $\vec{v}$ and the isotropic diffusion of pores, represented by the second-order term in Equation (2).

Migration of pores via surface and bulk diffusion is included in Equation (2) for two reasons: i.) Migration of pores in fuel via surface diffusion has been theoretically demonstrated by Desai [14], and ii) the presence of the diffusion term changes the mathematical character of Equation (2) from purely hyperbolic (appropriate for modeling wave-like phenomena) to elliptic. In the temperature range of interest, the diffusion term has only a minor contribution to overall porosity redistribution, but it is included for completeness. Equation (2) is similar to other equations used to model pore migration found in many instances throughout the literature [15].

We also include the mechanics equation (3) to capture the effect of displacements in the domain. In this work, the displacements are indirectly coupled to porosity through the temperature field via the coefficient of thermal expansion. The effect of stress is included here to demonstrate that Equations (1)–(3) can be solved implicitly (fully coupled), and could potentially include a direct relationship between stress and pore migration if such a model were to be proposed in the future.

3.2. Pore velocity

Pore velocity, $\vec{v}$, is a highly uncertain quantity and has been the subject of a considerable amount of prior study [1,3,4,6,7,15–17]. For this work, we use the pore velocity formula proposed by Sens [4]:

$$\vec{v} = c_0\left(c_1 + c_2 T + c_3 T^2 + c_4 T^3\right)T^{-5/2} \times \Delta H P_0 \exp\left(-\frac{\Delta H}{RT}\right)\nabla T \tag{4}$$

where, T is temperature, ∇T is the temperature gradient, R is the universal gas constant. This model is based on vapor pressure P driving pore migration with the velocity given by $\vec{v} = N\Omega_T \frac{D}{RT}\nabla P$, where N is Avogadro's number, Ω_T is the molecular volume of UO_2, and D is the vapor diffusion coefficient. The velocity is aligned with the gradient of vapor pressure ∇P, and therefore the temperature

gradient since $\nabla P = \frac{\partial P}{\partial T}\nabla T$. The detailed derivation of the velocity Equation (4) is given in Sens' original paper [4]. The exponential, Arrhenius term describes the dependence of UO_2 vapor pressure P on temperature, with a pre-factor P_0 and a heat of vaporization ΔH. The temperature dependence $T^{-5/2}$ comes from $D\frac{\partial P}{\partial T}$. The polynomial term describes the temperature dependence of UO_2 molecular volume, with the constants $c_1, \ldots, c_4$ determined by experimental measurement of UO_2 density. The coefficient c_0 is just the product of many other constants used in the derivation. This model is consistent with the notion of pore transport as a consequence of vapor pressure variations in solid materials which produce repeated vaporization and condensation cycles.

3.3. The effect of porosity on thermal conductivity

We used the MOX fuel thermal conductivity model of Kato et al. [18] for the simulations in this work. In this model, the effective fuel thermal conductivity in W/m-K is given by

$$k = \frac{f(p)\left[\frac{1.541\times10^{11}}{T^{2.5}}\right]\exp\left(\frac{-1.522\times10^4}{T}\right)}{g(x, \mathrm{Am}, \mathrm{Np}, T)} \tag{5}$$

where

$$\begin{aligned} g(x, \mathrm{Am}, \mathrm{Np}, T) = {}& 1.595 \times 10^{-2} + 2.713x + \left(3.583 \right. \\ & \times 10^{-1}\Big)\mathrm{Am} + \left(6.317 \times 10^{-2}\right)\mathrm{Np} + (\\ & \left. - 2.625x + 2.493\right) \times 10^{-4}T \end{aligned} \tag{6}$$

and p is the fuel porosity (fraction of pores per unit volume), x is the stoichiometric deviation $(2 - x)$, Am is the americium content and Np is the neptunium content (weight fraction). The coefficient $f(p)$ in Equation (5) is defined by

$$f(p) = \frac{1-p}{1+p/2} \tag{7}$$

Although Equation (7) is included in the thermal conductivity equation found in Ref. [18], it is referred to as the Maxwell-Eucken equation [19,20] and is a common approach to modeling thermal conductivity degradation with increasing porosity assuming the pores conduct no heat. The porosity can vary between 0 (representing solid material with no pores) and 1 (representing empty space or voids). In Equation (7), when $p\to0$, $f(p)\to1$, and as $p\to1$, $f(p)\to0$. In practice, when $p > 0.95$, the value of the porosity in Equation (7) is artificially limited to 0.95 to avoid numerical difficulties in the energy conservation equation associated with $k\to0$. Limiting the effect of porosity in this fashion has a physical basis because Equation (7) over estimates thermal conductivity degradation with increasing porosity due to the fact that the pores are filled with gas and conduct some heat.

3.4. Heat generation

The volumetric heat source, q (W/m^3), in Equation (1) also varies with porosity. In these calculations, q is scaled by:

$$c(p) = \frac{1-p}{1-p_{\mathrm{initial}}} \tag{8}$$

In the initial configuration, $c(p) = 1$. As porosity changes throughout the domain, this scale factor reduces the effective volumetric heating as $p\to1$, and increases it as $p\to0$.

4. Demonstration calculations

Medvedev [21] first studied temperature-dependent pore migration in BISON based on experimental observations. This work is an extension of those early calculations. Porosity is now a primary variable in the simulations, and the models themselves incorporate established theory for estimating pore velocity and porosity-dependent fuel thermal conductivity.

4.1. Model description

In the following sections, details regarding the geometry, finite element mesh features, materials, initial and boundary conditions, and power history are documented.

4.1.1. Geometry and finite element mesh

For these calculations, we restrict the domain to the fuel pellet. We employ 1D axisymmetric geometry of unit axial length, or, described alternatively, the domain of this model is shaped like a right circular cylinder (a shape similar to a hockey puck). These assumptions allowed us to use a single line of 1D finite elements with total length equal to the radius of the fuel. Along this line we used 200 elements (first order elements). Note that the stress divergence equation (3) is solved assuming generalized plane strain, which means that out-of-plane (top or bottom of the fuel pellet) forces and displacements are uniform along the fuel radius. The fuel pellet radius is $R = 2.675 \times 10^{-3}$ m.

4.1.2. Material behavior

Linear elastic fuel is assumed in these calculations, and we note that while the effect of mechanical loads is not significant in these applications, they are nevertheless included here to demonstrate the capability. The material property values (in SI units) are:

- $\nu = 10^{-12}$ m^2/s
- $C = 120$ J/K-kg
- $\rho = 1.0662 \times 10^4$ kg/m^3
- The elastic modulus is 200 GPa and Poisson's ratio is 0.345.
- Coefficient of thermal expansion is 10^{-6} K^{-1}.
- The strain-free reference temperature for thermal expansion is 300 K.
- In Equation (6) the O/M ratio is 2 ($x = 0$), and Am = Np = 0.

The values for material constants used here are typical of oxide fuel and only required to be representative for the purpose of this demonstration. Similar material properties can be found in the MATPRO library of material properties [22]. The pore diffusion coefficient, ν, is uncertain, although the value selected here provided reasonable results and numerical stability. More discussion regarding numerical stability is included in Section 4.3.

4.1.3. Initial conditions, boundary conditions, and power history

To generate the thermal and mechanical boundary conditions for the porosity migration calculations in the fuel, a thermo-mechanics simulation of a fast reactor fuel pin was first run. This preparatory calculation included typical power, sodium coolant thermal/pressure boundary conditions, and physical dimensions. Average fuel surface temperature and pressure were extracted from this simulation at each time step and recast as boundary conditions in the form of functions of temperature/pressure vs. time. The details of this preparatory simulation are not included here, since the input parameters are typical, and similar conditions appear in other published works such as [23]. See Fig. 3a and b for the respective thermal and pressure boundary conditions that are applied to the energy conservation (1) and stress divergence (3) equations at the
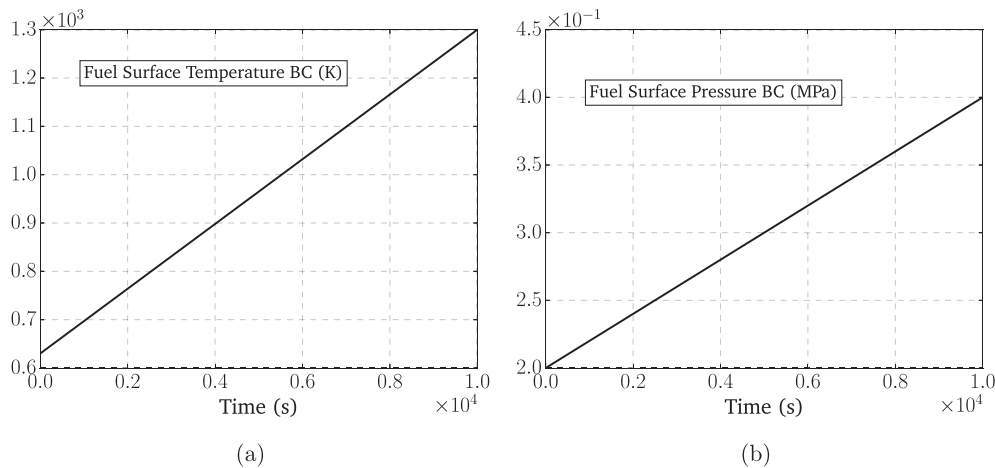
Fig. 3. Temperature (a) and Pressure (b) boundary conditions applied to fuel surface for the 1D axisymmetric fuel pellet. These functions were developed from an independent simulation of a fast reactor fuel pin in BISON. It's meant to be representative of the fuel surface temperature and pressure in a typical oxide fuel pin and used here to simplify the calculations for investigating pore migration.

fuel surface. For the porosity variable, the initial condition is set to $p_{initial} = 0.15$ everywhere, and a no flux boundary condition is applied at the fuel surface ($\frac{\partial p}{\partial n} = 0$, i.e. no pores cross the surface).

Axisymmetry is enabled by applying boundary conditions at the fuel center that specify zero flux for the temperature and porosity variables and zero displacement parallel to the radius. The model can be described as a hockey puck shape with the aforementioned temperature and pressure boundary conditions applied to the outer surface of the puck. The pressure applied at the top and bottom of the puck would act uniformly due to the generalized plane strain assumption. Note the ∇ operator in Equations (1)–(3) would take on cylindrical form. For the power history, the heating term is represented as a linear ramp from 0 to 5×10^4 W/m over 10^4 seconds.

4.2. Calculation results

Results from the simulation end time are shown in Fig. 4a-f. We found that typical run times for these 1D simulations with 604 degrees of freedom were less than 1 minute in wall clock time when run with 1 processor.

Fig. 4a shows that $p \approx 1$ from the fuel center through about 20% of the radius. This corresponds to the central void region in Fig. 1. At the edge of the void is a region of higher density (low porosity) material, followed by a region of gradually increasing porosity, and finally a region corresponding to $p = p_{initial}$. These regions are qualitatively similar to the images of Figs. 1 and 2.

Fig. 4b shows the temperature profile through the fuel radius at the simulation end time. The "standard" parabolic temperature profile (in cases where pore migration is not modeled) is replaced by a region of constant temperature followed by a region with a parabolic profile. The constant temperature region for $r/R \leq 0.2$ corresponds to the location of the central void. Fig. 4c shows the temperature gradient vs. fuel radius. The flat region from the fuel center to about 20% of the radius is evident and coincides with the void. The small oscillation seen at $r/R \approx 0.2$ corresponds to large changes in thermal conductivity (see Fig. 4e). This oscillation is characteristic of finite element formulations of the energy conservation problem with large changes in thermal conductivity, and can be reduced by increasing the finite element mesh density or employing adaptive mesh refinement.

Fig. 4d shows pore velocity vs. normalized radial location. The same oscillation at $r/R \approx 0.2$ can be seen, similar to that of Fig. 4c

and is due to the fact that the pore velocity is a function of thermal gradient (see Equation (4)). We note that the pore velocity is strictly negative since the temperature gradient is negative, and it takes on its minimum value around $r/R = 0.4$, which suggests that the pores are moving fastest just before reaching the central void region. Under the modeling assumptions in the present work, the maximum pore velocity magnitude is on the order of tens of microns per second, which is reasonable and consistent (as expected) with other sources such as Sens [4].

The change in fuel thermal conductivity as a function of normalized radial distance is shown in Fig. 4e. The thermal conductivity is inversely proportional to the porosity due to the $f(p)$ coefficient defined in Equation (7). Fig. 4f shows the fission rate vs. normalized radial coordinate. This curve is similar to the thermal conductivity, and is consistent with the expectation that no power generation is occurring in the central void region. Fig. 4a, e, and 4f show the tightly coupled nature of the relationship between porosity, thermal conductivity, and power generation.

4.3. Spatiotemporal studies

Accurate porosity migration calculations are very sensitive to computational mesh density. This is because of the large change in porosity near the void edge and the corresponding large number of elements required to capture the steep porosity gradient seen in Fig. 4a. Spatiotemporal calculations were run to demonstrate convergence of the numerical method. Fig. 5 shows porosity, p, as a function of normalized radial coordinate for three finite element models with increasing mesh density. The results converge as the number of elements increase. Use of higher order finite elements improves this convergence, but here, results are limited to finite elements of first order.

When the cell Peclet number, which is defined as:

$$Pe_h = \frac{|\vec{v}|h}{2\nu},\tag{9}$$

where $|\vec{v}|$ is the pore velocity magnitude, h is the finite element size, and ν is the Fickian diffusion coefficient of the pores, is larger than 1, the pore transport equation is said to be "advection-dominated." It is well-known that Galerkin finite element formulations of advection-dominated transport equations can exhibit spurious numerical oscillations. In the present simulation, we have
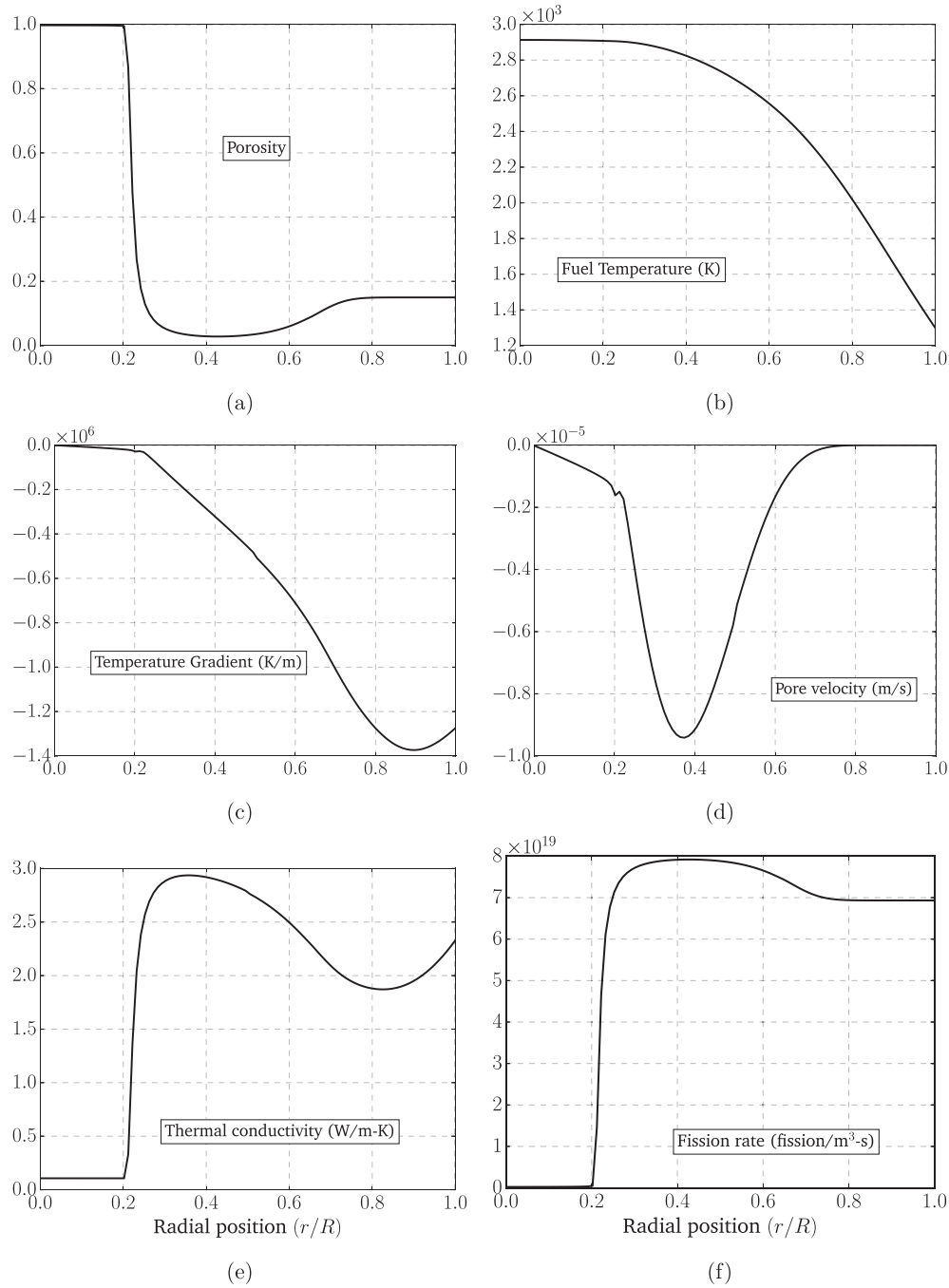
Fig. 4. Calculation results for the 1D axially symmetric fuel pellet at 10^4 seconds (end of simulation). In (a), $p \approx 1$ for $0 \leq r/R \leq 0.2$; this corresponds to the central void region. For $0.2 \leq r/R \leq 0.7$, $p < p_{\text{initial}}$, i.e. the fuel is more dense in this region, which is consistent with experimental observations. In (b), the effect of porosity is to "flatten" what would otherwise be a parabolic temperature profile throughout the pellet. Temperature gradient vs. fuel radius is shown in (c), where the small oscillation seen at $r/R \approx 0.2$ corresponds to large changes in thermal conductivity. In (d), there is a small oscillation in the pore velocity field which arises due to the corresponding discontinuity in the temperature gradient at this point. In (e) and (f), we observe that the thermal conductivity and power generation are both low where the porosity is high, and vice-versa.

$Pe_h \approx 100{-}500$, and do indeed observe numerical oscillations, although their amplitude is damped under mesh refinement. Furthermore, we've found that activating the diffusion term only when pore velocity is non-zero results in lower amplitude oscillations. A stabilized finite element formulation based on the Streamline Upwind/Petrov−Galerkin (SUPG) method [24] could also be employed in order to damp these oscillations on coarser grids.

A temporal study was also performed in which the time step was held constant throughout the simulation. We found that a time step size larger than 50 s resulted in non-convergence of the numerical scheme in this particular problem. In a typical simulation, the time step would automatically decrease to account for rapid transients in the field variables, then increase as the solution approaches steady state. We believe that an adaptive time step selection algorithm is essential for any fuel performance code that attempts to simulate pore migration in a fully-coupled manner.
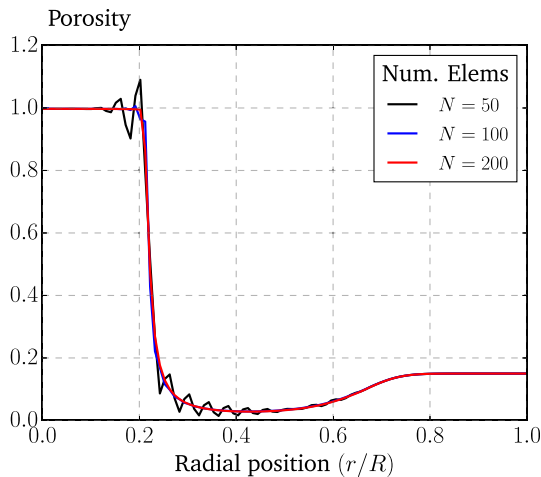
Furthermore, temporal convergence was demonstrated. The

Fig. 5. For the purpose of demonstrating spatial resolution, shown here are calculation results for the porosity field variable vs. normalized radial position from the 1D axially symmetric simulation of the fuel pellet at 10^4 seconds (end of simulation) for meshes with $N = 50$ (black), 100 (blue), and 200 (red) elements in the radial direction. (For interpretation of the references to colour in this figure legend, the reader is referred to the Web version of this article.)

smallest time step in the preceding calculations was 10 s, so an additional simulation was run with a fixed time steps of 5 s. The results were nearly identical.

4.4. Solid vs. annular fuel

Use of annular fuel in some reactors motivated a comparison between annular and solid fuel pellets. In the calculations for annular fuel, the inner radius is $r = 0.7 \times 10^{-3}$ m (recall the fuel outer radius is $R = 2.675 \times 10^{-3}$ m).

Results for annular pellets are similar to those of solid pellets in terms of the predicted thermal conductivity and pore distribution, but the central void diameter is quite different in the two cases. The annular pellet begins the simulation with an inner radius, and therefore the thermal gradient is not as steep at the beginning of the simulation. It takes time for the void in solid fuel to form, grow, and reach the initial inner radius size of the annular fuel. Fig. 6 shows central void radius vs. linear heat generation rate for the solid and annular fuel cases. Pore migration to the inner surface of the annular fuel is slow. Once a sufficient density of pores accumulates at the inner surface, the central void growth continues with a similar growth rate for the solid and annular fuel. The criteria for determining central void size was chosen to be the location at which $p \geq 0.3$. This choice is somewhat subjective, and selecting radial locations in this manner likely contributes to the change in slope seen in Fig. 6 for the solid fuel case.

4.5. Void formation progression with power: calculation and experiment

Central void formation in oxide fuel is known to be a strong function of rod linear power. As shown in Fig. 7a, the diameter of the central void increases with an increase of linear heat generation (LHGR) [23]. To investigate response of the newly implemented pore migration model in BISON, a series of calculations of radial porosity distribution were performed for LHGR of 20−50 kW/m in 5 kW/m increments. Results of these calculations are shown in Fig. 7b. It was found that BISON has reproduced the *trend* of increasing central void with an increase of LHGR. Future work will be focused on extensive modeling of fast reactor oxide fuel
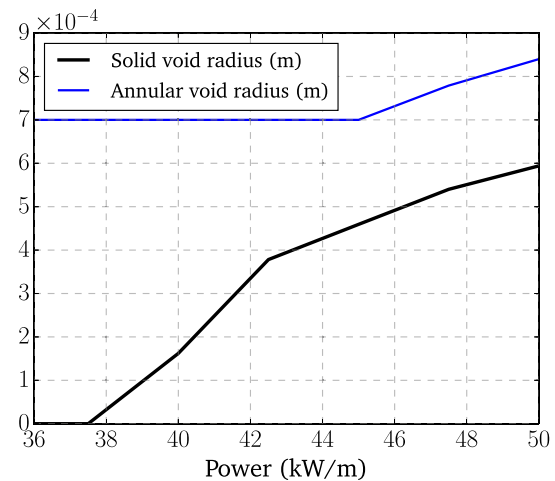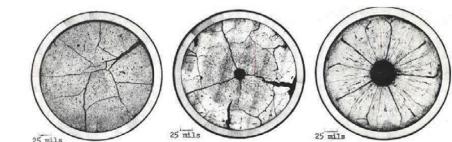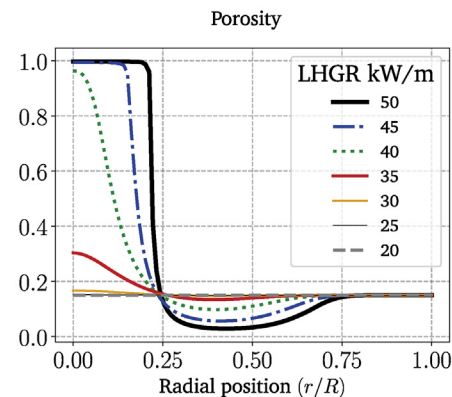

Fig. 6. Calculation results from 1D axisymmetric simulations of solid and annular fuel, showing the differences in central void growth between the two fuel shapes at the end of simulation.

(a) Micrographs of void formation at 19.7 kW/m (left), 31.1 kW/m (middle), and 46.0 kW/m (right) [23].

(b) BISON simulation results at different linear powers showing the effect of LHGR on radial porosity distribution.

Fig. 7. Top: micrographs of void formation at different linear powers [23]. Bottom: BISON Calculation for the porosity field variable vs. normalized radial position from the 1D axially symmetric simulation of the fuel pellet at varying LHGRs. This shows the pore migration model adequately reproduces the trend of increasing void diameter with increasing power.

irradiation experiments and comparing measured central void diameter with that calculated using BISON.

4.6. Rate effects

Three rate simulations were run to study the effect of power ramp rate on porosity migration and temperature in the pellet. The previously described 1D axisymmetric model of the fuel pellet was used for these calculations. The linear heat generation was ramped

from 0 to 5×10^4 W/m in successively shorter times resulting in power ramp rates of 5, 50, and 500 W/m-s. In other words, the linear heat generation rate, 5×10^4 W/m, is reached in 10^4, 10^3, and 10^2 seconds respectively. The temperature and porosity results of this study are shown in Fig. 8a and b. The calculations indicate that as the power ramp rate is increased, the fuel temperature gets higher and a correspondingly smaller central void is formed. Our conclusion is that there is a threshold ramp time for the central void to form. The pore migration velocity is finite; therefore, it is possible to bring fuel to full power before the pores begin arriving to the fuel centerline. The significance of this is as follows: First, because formation of the central void prevents fuel from melting, short ramp times, and the corresponding positive difference between the rate at which heat transfers vs. the rate at which pores migrate, may cause fuel to melt. Second, this establishes a basis for performing an experiment in a recently restarted TREAT reactor where the effect of reactor ramp time on the fuel microstructure can be investigated to validate pore migration velocity values calculated by this model.

4.7. Multidimensional effects

A 2D calculation was also run to demonstrate the effects of fuel being offset within the cladding. The expectation is that an offset fuel pellet will get hotter on the side with the larger pellet/clad gap, and, consequently, the central void formation will also be offset. The 2D calculation was performed on a mesh with a fuel pellet radius of $R = 2.675 \times 10^{-3}$ m, and a 57.5×10^{-6} m thick cladding with a 105×10^{-6} m gap between the fuel and cladding. The thermal conductivity, specific heat, and density of the cladding were: 15 W/m-K, 470 J/K-kg, and 8×10^3 kg/m^3 respectively. The properties of the fuel are described in prior sections. This calculation was limited to energy conservation (Equation (1)) and porosity migration (Equation (2)). Because of the change in geometry from 1D axisymmetric, as described previously, to 2D Cartesian, Equations (1) and (2) would take on the corresponding form. The fuel and cladding were thermally coupled via a meshless contact algorithm with a gap conductivity of 0.2 W/m-K. A Dirichlet thermal boundary condition of 600 K was applied to the surface of the cladding. Simulations were run with both concentric fuel (uniform gap size of

105×10^{-6} m) and fuel offset relative to the cladding axis by 80×10^{-6} m. Power was ramped from 0 to 37 kW/m in 10^4 seconds. Symmetry was utilized in the direction orthogonal to the direction of the offset and the corresponding boundary conditions were used. Results, reflected about the axis of symmetry, are shown in Fig. 9a and b where the offset high temperature and corresponding offset void formation are demonstrated, respectively. A micrograph showing similar offset behavior is shown in Fig. 10 for a qualitative comparison between calculation and measurement.

When comparing the calculations shown in Fig. 9b to the micrograph in Fig. 10, it is interesting to note that in addition to the offset void, we see that the shape of the void is similar and that it is more elliptical than circular. Also, the ellipse's major axis is oriented orthogonally to the temperature gradient according to the calculations shown in Fig. 9b. Results from the concentric simulations are shown in Fig. 9c and d.

Multidimensional calculations could be extended to 3D, where a situation such as an axially and circumferentially varying temperature profile in a fuel pin (i.e. no symmetry) could be modeled accurately. It is important to note here the large mesh density requirement for such calculations. For a 2D mesh utilizing symmetry, like those shown in shown in Fig. 9a and b, the number of degrees of freedom was about 1.2×10^5 with wall clock run times of about 2×10^4 seconds when run with 36 processors. Going from 2D to 3D, a mesh density of 10 elements through the length of the fuel pellet would result in over 10^6 degrees of freedom and a wall clock time of roughly 2×10^5 seconds. In other words, for a modest increase in mesh size the simulation would take 10 times longer than the 2D case. Extending this to an entire fuel pin with hundreds of pellets, the demand for processing power increases immensely. Even so, running large 3D simulations with BISON is straightforward, the only limitation being run time and perhaps memory.

To address this issue, an approach similar to that of Spencer [25] could be used to reduce the size of the problem by having one section of a full length fuel rod modeled with 3D elements, to capture the 3D effect of interest, while the remaining section is modeled with 2D axisymmetric elements. Automated mesh refinement methods as well as stabilized finite element formulations of the porosity advection-diffusion equation could also be employed to reduce the mesh density requirements.
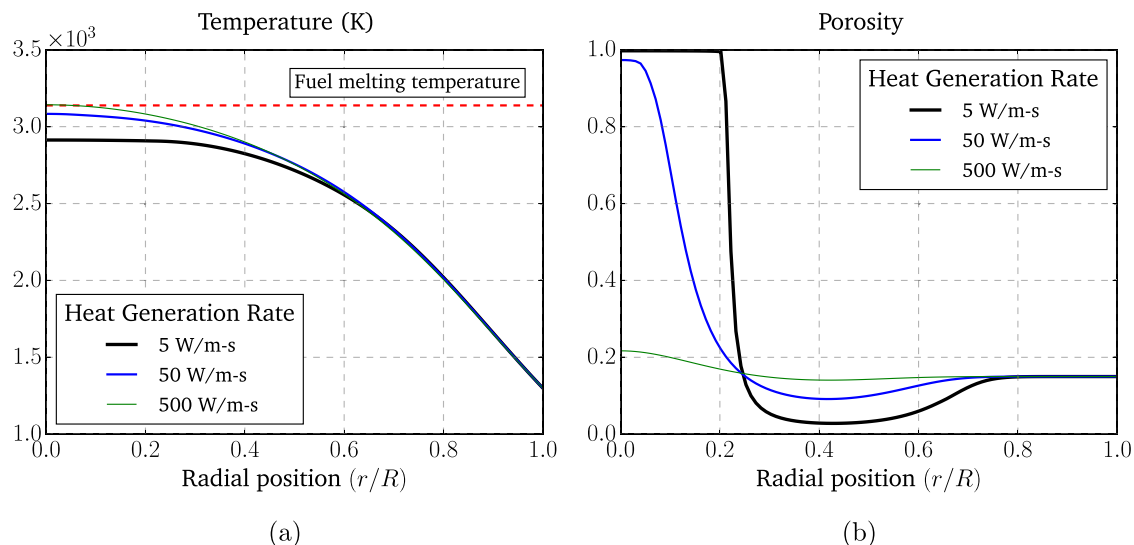
Fig. 8. Calculation results showing temperature (a) and porosity (b) vs. normalized radial position for power ramp rates of 5, 50, and 500 W/m-s to a peak LHGR of 5×10^4 W/m on the 1D axisymmetric pellet. The calculations indicate that as the power ramp rate is increased, the fuel temperature gets higher and a correspondingly smaller central void is formed.
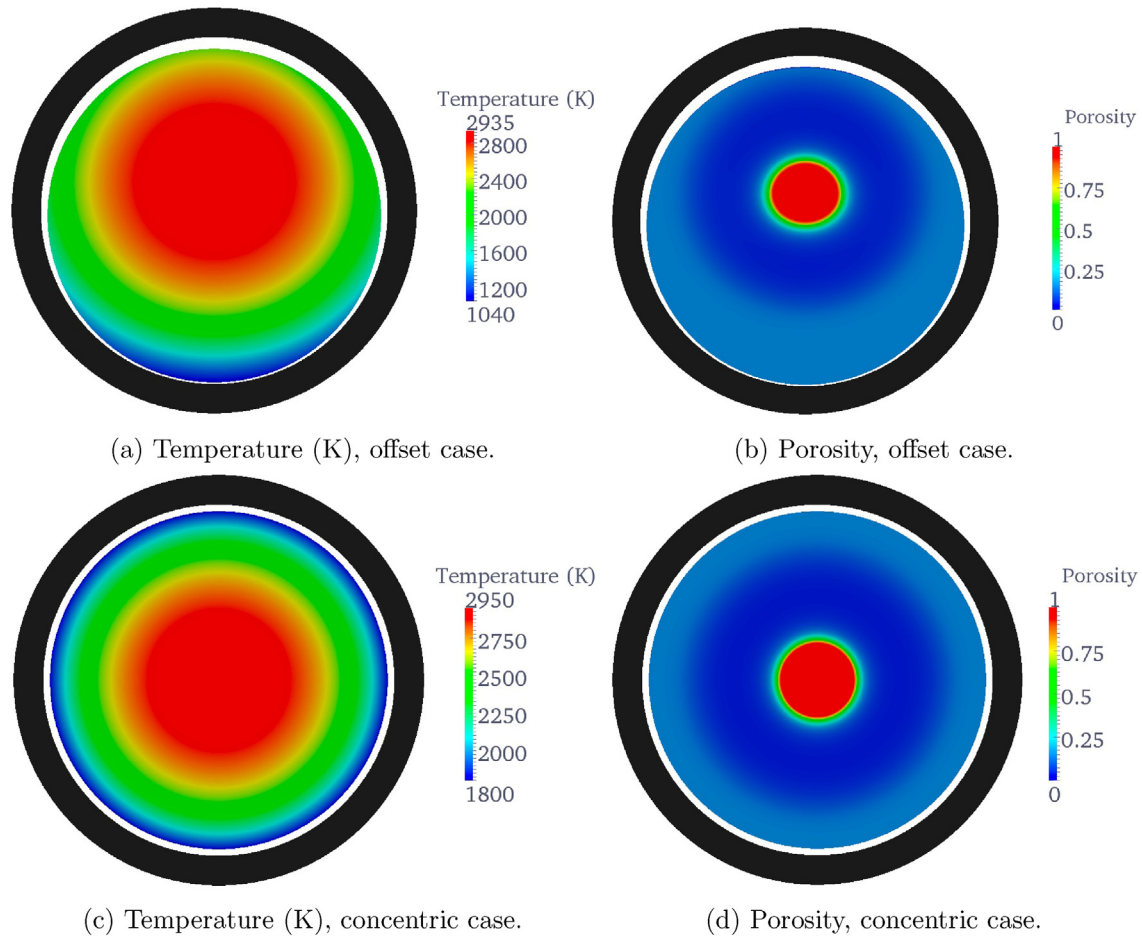
(a) Temperature (K), offset case.

(b) Porosity, offset case.

(c) Temperature (K), concentric case.

(d) Porosity, concentric case.

Fig. 9. 2D calculation showing temperature and porosity contours in a restructured fuel pellet in both offset (a, b) and concentric (c, d) positions relative to the cladding. The as-fabricated porosity was 15%. Power was ramped from 0 to 37 kW/m in 10^4 seconds. Cladding exterior was held at 600 K. The pellet and cladding were thermally coupled using a meshless contact approach. For the offset case, the contour plot shows the peak temperature and porosity is offset from the geometric center, which is expected due to the offset fuel pellet within in the cladding. The offset position of the fuel pellet creates a gap that is larger on one side, resulting in correspondingly higher temperatures in the direction of the larger gap. Also note the elliptic shape of the central void with the major axis orthogonal to the thermal gradient. The offset and shape of this void is qualitatively similar to the micrograph shown in Fig. 10.
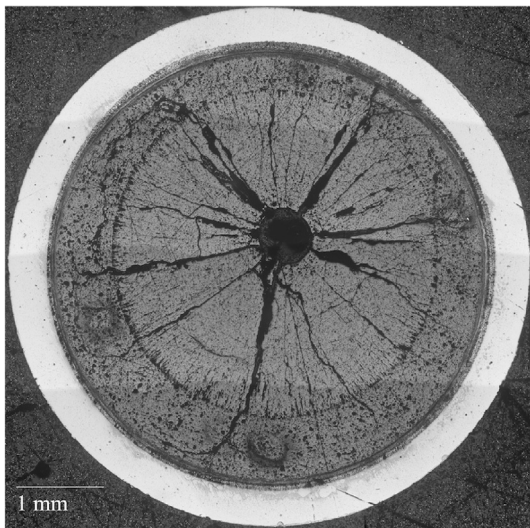

Fig. 10. Micrograph from Chichester [26]. The fuel composition is $U_{0.75}Pu_{0.20}Am_{0.03}Np_{0.02}O_{1.98}$ irradiated at an average power of 321 W/cm. Compare the micrograph shown here to the porosity field calculation in Fig. 9 for the offset case. Both figures show an elliptic-shaped central void offset from the geometric center.

Multidimensional considerations are important because accurate fuel temperature calculations enable designs that prevent fuel melting and predict if and when fuel restructuring will occur. Using approaches that are restricted to 1D or 2D misses these potential issues.

5. Extension of recent work

Recently, Vance [15] has shown lower length scale calculations for the velocity and shape of an *individual* pore as it moves toward the fuel center by using Sens' pore velocity formula (Equation (4)). Vance prescribed a parabolic temperature distribution through the fuel pellet for these calculations, but suggested that future work could include a direct calculation of the temperature field, which is exactly what we've done in the simulations presented in prior sections. The reason this is important is because these direct, point-to-point calculations of temperature in the presence of a porosity field will be different than the parabolic temperature distribution that Vance prescribed for his calculations. To illustrate this point, an additional simulation of the 1D axisymmetric model (described previously) was run *sans* the porosity variable, yet retaining the calculation for pore velocity based on temperature and temperature gradient. The reader is cautioned on this point because of
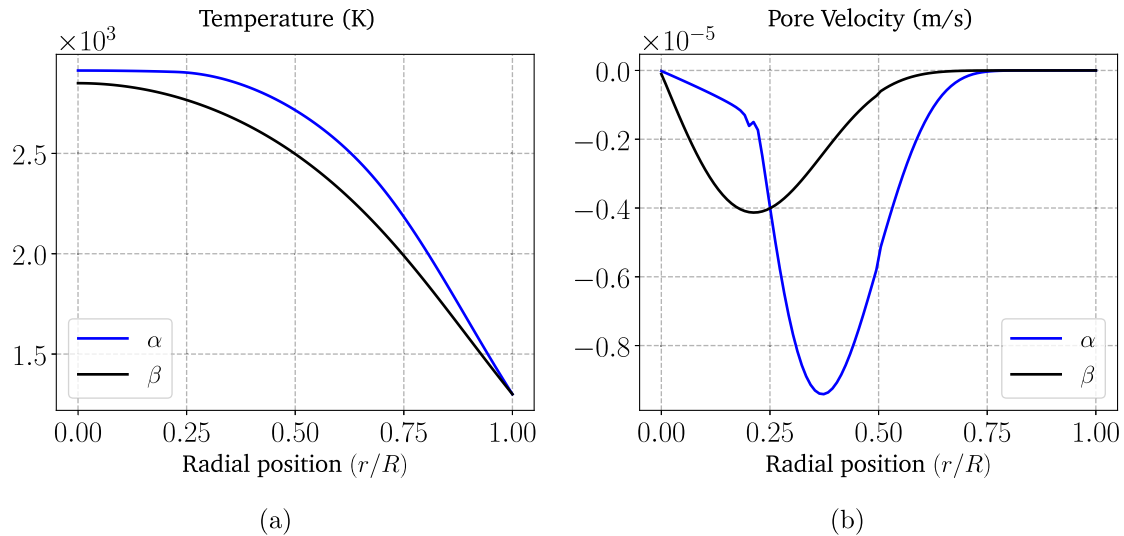
Fig. 11. Temperature (a) and pore velocity (b) vs. normalized radial position from the 1D axisymmetric model with (α) and without (β) the effect of porosity on temperature.

potential confusion concerning the calculation of pore velocity while omitting the porosity field variable. Due to the absence of the porosity variable, the temperature distribution will be parabolic, similar to Vance's calculations, and will yield a pore velocity calculation independent of the effect of porosity. Results for temperature and pore velocity as a function of normalized pellet radius, for simulations with (α) and without (β) the effect of porosity, are shown in Fig. 11a and b respectively.

6. Conclusions

Modeling porosity as a field variable that is fully coupled to temperature has been shown here to realistically capture the important effect of porosity on typical fuel performance calculations. The approach outlined here demonstrates, specifically, how power generation, thermal conductivity, fuel temperature, and pore velocity itself are all affected by porosity. A reasonable prediction of central void formation and growth and the corresponding effect on fuel temperature is also demonstrated. Furthermore, the importance of multidimensional (e.g. offset fuel) effects in fuel pellets can now be evaluated. These modeling considerations should play a vital role in licensing.

Due to the large change in porosity near the central void boundary, relatively large finite element mesh densities are required to accurately resolve the fuel/void interface. This limitation can of course impact the size of the overall finite element model which can be employed, depending on available computational resources. As discussed previously, a hybrid 2D/3D model, automated mesh refinement, and stabilized finite element methods may also help address this limitation by reducing the overall model size.

The uncertainty surrounding the pore velocity/temperature correlation has been studied [4] and greatly affects the results shown here. In this work, we've considered ceramic fuel (UO_2 and MOX) in general. Incorporating other approaches and details for pore velocity calculations is ongoing with colleagues from the Japan Atomic Energy Agency (JAEA), who have shown that detailed equations for vapor pressure [27] and O/M ratio [28] regarding the constituents of fuel (UO_2 vs. MOX) are very important when calculating pore velocity.

Other follow-on work that is worth pursuing is the relationship between lower-length scale calculations and the corresponding influence on engineering-scale calculations. For example, the relationship between pore shape at the meso-scale [15] and pore velocity at the engineering scale, or how fuel cracking is affected by restructuring.

For a model to be useful, validation is critical. Assessment of the work presented here could be done with experiments that measured the void growth rate as a function of power and power ramp rate, as discussed in Section 4.6 with destructive or non-destructive fuel imaging tests.

References

[1] D.R. Olander, Fundamental Aspects of Nuclear Reactor Fuel Elements, Technical Information Center, Energy Research and Development Administration, 1976.
[2] S.L. Seiffert, UO_2 fuel behavior under power-cooling-mismatch conditions, Tech. Rep.. NUREG/CR-2262, Idaho National Engineering Laboratory, 1981, pp. 42–43.
[3] F.A. Nichols, Theory of columnar grain growth and central void formation in oxide fuel rods, J. Nucl. Mater. 22 (2) (1967) 214–222, https://doi.org/10.1016/0022-3115(67)90031-1.
[4] P.F. Sens, The kinetics of pore movement in UO_2 fuel rods, J. Nucl. Mater. 43 (3) (1972) 293–307, https://doi.org/10.1016/0022-3115(72)90061-X.
[5] I.W. Vance, Computer Simulation of Pore Migration Due to Temperature Gradients in Nuclear Oxide Fuel, Master's thesis, University of Arkansas, Fayetteville, 2017, http://scholarworks.uark.edu/etd/1943.
[6] T. Ozawa, T. Abe, Development and verifications of fast reactor fuel design code CEPTAR, Nucl. Technol. 156 (2006) 39–55, https://doi.org/10.13182/NT156-39.
[7] A. Karahan, Modeling of Thermo-mechanical and Irradiation Behavior of Metallic and Oxide Fuels for Sodium Fast Reactors, Ph.D. thesis, Massachusetts Institute of Technology, Jun. 2009, https://tinyurl.com/y72vqvbn.
[8] J.C. Melis, L. Roche, J.P. Piron, J. Truffert, GERMINAL — a computer code for predicting fuel pin behaviour, J. Nucl. Mater. 188 (1992) 303–307, https://

doi.org/10.1016/0022-3115(92)90488-7.

[9] J.C. Melis, J.P. Piron, L. Roche, Fuel modeling at high burn-up: recent development of the GERMINAL code, J. Nucl. Mater. 204 (1993) 188—193, https://doi.org/10.1016/0022-3115(93)90216-L.

[10] V.Z. Jankus, R.W. Weeks, LIFE-II — a computer analysis of fast-reactor fuel-element behavior as a function of reactor operating history, Nucl. Eng. Des. 18 (1) (1972) 83—96, https://doi.org/10.1016/0029-5493(72)90038-6.

[11] T. Uwaba, T. Mizuno, J. Nemoto, I. Ishitani, M. Ito, Development of a mixed oxide fuel pin perfromance analysis code "CEDAR": models and analyses of fuel pin irradiation behavior, Nucl. Eng. Des. 280 (2014) 27—36, https://doi.org/10.1016/j.nucengdes.2014.08.032.

[12] R.L. Williamson, J.D. Hales, S.R. Novascone, M.R. Tonks, D.R. Gaston, C.J. Permann, D. Andrš, R.C. Martineau, Multidimensional multiphysics simulation of nuclear fuel behavior, J. Nucl. Mater. 423 (1—3) (2012) 149—163, https://doi.org/10.1016/j.jnucmat.2012.01.012.

[13] D.R. Gaston, C.J. Permann, J.W. Peterson, A.E. Slaughter, D. Andrš, Y. Wang, M.P. Short, D.M. Perez, M.R. Tonks, J. Ortensi, L. Zou, R.C. Martineau, Physics-based multiscale coupling for full core nuclear reactor simulation, Annals of Nuclear Energy, Special Issue on Multi-Physics Modelling of LWR Static and Transient Behaviour 84 (2015) 45—54, https://doi.org/10.1016/j.anucene.2014.09.060.

[14] T.G. Desai, P.C. Millet, M. Tonks, D. Wolf, Atomistic simulations of void migration under thermal gradient in UO₂, Acta Mater. 58 (2010) 330—339, https://doi.org/10.1016/j.actamat.2009.09.011.

[15] I.W. Vance, P.C. Millet, Phase-field simulations of pore migration and morphology change in thermal gradients, J. Nucl. Mater. 490 (2017) 299—304, https://doi.org/10.1016/j.jnucmat.2017.04.027.

[16] D.R. De Halas, G.R. Horn, Evolution of uranium dioxide structure during irradiation of fuel rods, J. Nucl. Mater. 8 (2) (1963) 207—220, https://doi.org/10.1016/0022-3115(63)90036-9.

[17] W.J. Lackey, F.J. Homan, A.R. Olsen, Porosity and actinide redistribution during irradiation of (U,Pu)O₂, Nucl. Technol. 16 (1972) 120—142, https://doi.org/10.13182/NT72-A31181.

[18] M. Kato, K. Maeda, T. Ozawa, M. Kashimura, Y. Kihara, Physical properties and irradiation behavior analysis of Np- and Am-bearing MOX fuels, Nucl. Sci.

Technol. 48 (4) (2011) 646—653, https://doi.org/10.1080/18811248.2011.9711745.

[19] J.C. Maxwell, A Treatise on Electricity and Magnetism, third ed., vol. I, Oxford University Press, 1892.

[20] A. Eucken, Allgemeine Gesetzmäßigkeiten für das Wärmeleitvermögen verschiedener Stoffarten und Aggregatzustände, Forschung auf dem Gebiete des Ingenieurwesens 11 (1) (1940) 6—20, https://doi.org/10.1007/BF02584103.

[21] P. Medvedev, Status of the B-14 experiment modeling using BISON, in: American Nuclear Society Conference Proceedings, vol.113, 2015.

[22] SCDAP/RELAP5-3D Code Manual, Volume 4: MATPRO a Library of Materials Properties for Light-water-reactor Accident Analysis, Tech. Rep. INEEL/EXT-02-00589, Idaho National Engineering and Environmental Laboratory, 2003.

[23] Y.S. Tang, R.D. Coffield, R.A. Markley, Thermal analysis of liquid-metal fast breeder reactors, American Nuclear Society, La Grange Park, Illinois 39 (1978) 219—225.

[24] A.N. Brooks, T.J.R. Hughes, Streamline Upwind/Petrov—Galerkin formulations for convection dominated flows with particular emphasis on the incompressible Navier—Stokes equations, Comput. Meth. Appl. Mech. Eng. 32 (1—3) (1982) 199—259, https://doi.org/10.1016/0045-7825(82)90071-8.

[25] B.W. Spencer, R.L. Williamson, D.S. Stafford, S.R. Novascone, J.D. Hales, G. Pastore, 3D modeling of missing pellet surface defects in BWR fuel, Nucl. Eng. Des. 307 (2016) 155—171, https://doi.org/10.1016/j.nucengdes.2016.07.008.

[26] H.J.M. Chichester, Post-irradiation Examination of AFC-2B and AFC-2C Experiments, Tech. Rep. INL/LTD-12—26154, Idaho National Laboratory, 2012.

[27] Y. Ikusawa, T. Ozawa, S. Hirooka, K. Maeda, M. Kato, S. Maeda, Development and verification of the thermal behavior analysis code for MA containing MOX fuels, in: Proceedings of the 22nd International Conference on Nuclear Engineering (ICONE22), Prague, Czech Republic, 2014, https://doi.org/10.1115/ICONE22-30005. V001T02A001 (6 pages).

[28] M. Kato, M. Watanabe, T. Matsumoto, S. Hirooka, M. Akashi, Oxygen potentials, oxygen diffusion coefficients and defect equilibria on nonstoichiometric (U,Pu)O₂±ₓ, J. Nucl. Mater. 487 (2017) 424—432, https://doi.org/10.1016/j.jnucmat.2017.01.056.